A Highly Efficient and Stable Oxygen Reduction Reaction on Pt/CeOx/C Electrocatalyst Obtained via a Sacrificial Precursor Based on a Metal-Organic Framework

Yun Luo, Laura Calvillo, Carole Daiguebonne, Maria K. Daletou, Gaetano Granozzi, Nicolas Alonso-Vante

A highly efficient and stable oxygen reduction reaction on Pt/CeO$_x$/C electrocatalyst obtained *via* a sacrificial precursor based on a metal-organic framework

Yun Luo[a], Laura Calvillo[b], Carole Daiguebonne[c], Maria K. Daletou[d], Gaetano Granozzi[b], Nicolas Alonso-Vante[a,]

[a] IC2MP, UMR-CNRS 7285, University of Poitiers, 4 rue Michel Brunet, 86022 Poitiers, France
[b] Department of Chemical Sciences, University of Padova, Via Marzolo 1, 35131 Padova, Italy
[c] INSA, UMR-CNRS 6226, 20 Avenue des Buttes de Coësmes, 35708 Rennes, France
[d] Foundation of Research and Technology, Hellas-Institute of Chemical Engineering Science, Stadiou Str., Platani Rion, Patras GR-26504, Greece

Graphical abstract
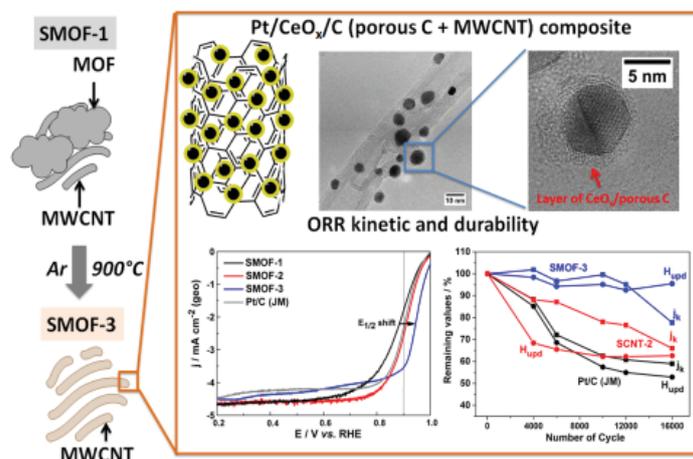
Highlights:

- Metal-Organic Framework (MOF) was applied for the in-situ formation of $Pt/CeO_x/C$ composite.

- $Pt/CeO_x/C$ morphology was unique since Pt NPs are in close contact with CeO_x.

- ORR activity and stability were improved due to the strong interaction of Pt with CeO_x.

- $Pt/CeO_x/C$ cathode showed enhanced performance in homemade H_2/O_2 micro laminar flow fuel cell.

Abstract:

Advanced Pt/CeO$_x$/C nanocomposite, where C = porous carbon and multi-walled carbon nanotube (MWCNT), was synthesized using a precursor based on Ce-containing metal organic framework (MOF), *via* carbonyl chemical route, followed by heat-treatment at 900 °C under argon atmosphere. Based on the analyses of powder X-ray diffraction (*p*XRD) data, and *via* the Williamson-Hall method, the lattice parameter, stacking fault and micro-strain values on Pt/CeO$_x$/C was found to decrease, whereas the crystallite size increased with respect to the as-prepared sample. Combined with the results of transmission electron microscopy (TEM), these changes were related to the *in-situ* formation of intimately contacted Pt/CeO$_x$ nanoparticles (NPs), well-dispersed onto MWCNT support. However, both the *p*XRD and TEM results showed that the Pt NPs were agglomerated upon heating and finally detached from the support in the MOF-free samples. Thus, MOF could protect Pt nanoparticles (NPs) from agglomeration at high temperature. The X-ray photoelectron spectroscopy (XPS) showed that the Pt surface was less oxidized in Pt/CeO$_x$/C nanocomposite in comparison to as-prepared and MOF-free samples. Moreover, only the Ce^{3+} was detected in the nanocomposite. These facts together with Raman spectroscopy and surface electrochemistry experiments assessed the stabilization of the electronic state of Pt^0 and Ce^{3+} via the interaction between Pt and CeO$_x$. In addition, enhanced catalytic activity towards the oxygen reduction reaction (ORR) was observed in acid medium. The specific and mass activity at 0.9 V/RHE on Pt/CeOx/C were *ca*. 1279 μA cm$^{-2}_{Pt}$ and 870 mA mg$^{-1}_{Pt}$, respectively, *ca*. 10 − 11 fold higher than commercial Pt/C (Johnson Matthey, JM) in half-cell. Accelerating durability tests (ADT), after 16,000 potential cycles, demonstrated higher stability of Pt/CeO$_x$/C in contrast to oxide-free and Pt/C (JM) catalyst. Compared with other homemade or

commercial Pt/C (JM) cathodes, the innovative cathode catalyst showed enhanced cell performance in a H_2/O_2 micro-laminar flow fuel cell system.

KEYWORDS: MOF, Pt nanoparticles, Pt/CeO$_x$/C nanocomposite, ORR, Oxides

1. Introduction

The sluggish kinetics of the oxygen reduction reaction (ORR) occurring at the cathode of fuel cells (FCs) represent a real challenge which is actually addressed by a fine tailoring of new ORR catalysts. Pt-based catalysts, mostly applied and studied for their high efficiency with respect to other Pt-free catalysts in acid medium [1], consist of Pt nanoparticles (NPs) supported onto different substrates, e.g. carbon, oxides and carbon/oxides composite substrates [2]. However, a big issue is associated to the high cost and limited availability of Pt. In order to significantly reduce the amount of Pt loading, several strategies have been undertaken, e.g. alloying Pt with other metals. Recently, Pt$_3$Y alloy was theoretically predicted as the most efficient and stable catalyst for ORR [3]. This expectation was confirmed on a Pt$_3$Y bulk electrode tested in acid medium [3, 4]. Pt$_5$Gd bulk alloy also showed excellent ORR activity and stability [5], implying that in general Pt alloys based on rare earth (RE) elements might be good candidates to improve the Pt catalytic performance in acid medium. Since then, many efforts have been devoted, by different research groups, to the synthesis of Pt NPs containing RE elements [6-8]. However, up to now, no evidence of the formation of Pt-RE nanoalloys *via* chemical routes has been obtained, even at high temperature, e.g. 900 °C [6]. The only exception was the Pt$_x$Y nanoalloy prepared *via* a physical method, using magnetron sputter agglomeration gas [9]. By employing the chemical route, instead, a large amount of RE oxides (RE = Y and Gd) was confirmed to be

4

present on the Pt NPs surfaces [7]. However, it is very interesting to note that also RE oxides can induce a positive effect onto Pt NPs, thus enhancing the ORR process [6-8]. In previous works, we demonstrated that the ORR activity and stability of Pt-M_2O_3/C (M=Y and Gd; C= Vulcan XC-72) can be increased after heat-treatment (HT) [10]. Such a phenomenon has been associated to Pt surface defects induced by the RE oxides upon heating [11]. However, we have found that Pt-M_2O_3/C catalysts, prepared from MCl_3 precursors, *via* the carbonyl chemical route [12], are agglomerated if HT is higher than 500 °C, leading to reduction of the Pt active surface and thus to a lower ORR activity. It is then necessary to tailor novel process to produce Pt-M_2O_3/C catalysts, protecting Pt NPs from agglomeration at temperatures higher than 500°C.

Metal-organic frameworks (MOFs) [13], known also as coordination polymers, are crystalline micro- or macro-porous materials, constructed by metallic ions that act as lattice nodes and are held in place by multidentate organic ligands. They have been studied in gas-separation [14], storage [15], luminescence [16], magnetism [17] and catalysis [18]. Regarding their application in catalysis, there are two main trends, i.e. their direct utilization as a catalyst [19, 20] or as a support/host for metal NPs [21]. In the former case, the ligands serve for tailoring the charge of the metal centers responsible as catalytic sites. In the latter case, noble metal NPs could be captured or supported by a MOF [21], which represent the actual catalytic sites either in catalysis [22] and photocatalysis [23]. An alternative route concentrates on using a MOF as a sacrificial precursor to synthesize powder catalysts after heat-treatment at temperature higher than 600 °C, under inert atmosphere [24-28]. The MOF can be carbonized as oxide/carbon composite or porous carbon. For example, Fe/N/CF composite can be prepared based on MOF [25], The porous carbon from heat-treated from a nitrogen-containing isoreticular MOF was studied for its high porosity and capacitance [28]. Compared with applications in chemistry and photocatalysis,

a few works, devoted to the utilization of MOF in electrocatalysis, have been published. For instance, Loh *et al.* reported porphyrin-based MOF grafting on graphene for ORR in alkaline medium [29]. Kitagawa *et al.* prepared a MOF-based electrocatalyst for ethanol oxidation reaction in acid medium [13]. MOF sacrificial precursor at 900–1000 °C have been used to template Fe graphene/carbon-nanotubes nanocomposites, resulting in an efficient catalysts towards ORR [27]. However, none of these systems was studied as a Pt-based electrocatalyst for FCs systems, nor the catalytic sites, efficiency and stability were investigated, to the best of our knowledge, in detail.

In this work, we focus on the synthesis of novel nanocarbon composites with Pt-RE oxide NPs *via* a MOF sacrificial precursor and on the study of their activity and stability towards ORR. The Ce(HATPT)(ATPT)·nH_2O (ATPT= 2-aminoteraphthalate) MOF [30], hereafter denoted as MOF(Ce), was used as sacrificial precursor to prepare a nanocomposite Pt-CeO_x/C electrocatalyst. The choice of MOF(Ce) was based on the following reasons:

1) As a member of the Ln(HATPT)(ATPT)·nH_2O (Ln = La – Eu except Pm) family, MOF(Ce) estimated specific surface area is around 2100 $m^2\,g^{-1}$, which is one of the most porous MOF structures involving RE elements so far obtained [30]. According to the literature [24-28], one can anticipate that, after carbonization, the MOF(Ce) structure can be transformed at high temperature (e.g. 900 °C) into a porous carbon mixed with Ce oxide. This new oxide/carbon composite support is expected to impact on the electrochemical performance of the final electrocatalysts.

2) MOF(Ce) structure is solely composed of Ce^{3+} metal centers, which might eventually decompose into CeO_x. Recently, Uosaki *et al.* reported that Ce^{3+} was responsible for Pt^0 rich

6

NPs surface, resulting in enhanced ORR activity in acid [31], The authors explained the enhanced activity to the inhibition of surface Pt oxidation in presence of Ce^{3+} [31].

3) As reported previously [30] the herein adopted MOF structure starts to decompose at temperature higher than 400°C under nitrogen flux, resulting in a porous nanocarbon, which is expected to stabilize the Pt NPs against agglomeration.

Herein, we report the synthesis *via* carbonyl chemical route [12] of an innovative Pt/MOF(Ce)/MWCNT composite system, (where MWCNT= multiwall carbon nanotubes), which has been subsequently subjected to a heat-treatment at 900 °C to provide a final $Pt/CeO_x/C$ (C = porous carbon with MWCNT) nanocomposite electrocatalyst. The as-prepared and heat-treated samples, at 400 °C and at 900°C, are further designated as SMOF-1, SMOF-2 and SMOF-3, respectively. The impact of the MOF(Ce) was studied in detail, and compared to MOF-free samples, i.e. as prepared Pt/MWCNT composite (SCNT-1), heat-treated Pt/MWCNT at 400 °C (SCNT-2) and at 900°C (SCNT-3). A quite unique nanocomposite structure was found in SMOF-3, and its activity towards ORR was systematically studied. Finally, it was tested as a cathode catalyst in a micro-laminar flow fuel cell (μLFFC) in acid medium.

2. Experimental Section

2.1. Preparation of SMOFs and SCNTs samples.

The preparation of oxidized MWCNT was already described in the literature [32]. The micro-crystalline powder of MOF(Ce) was prepared *via* a published method [30]. The synthesis of SMOFs samples was realized *via* carbonyl chemical route. 72.1 mg $Na_2PtCl_6 \cdot 6H_2O$ (99.9 %, Alfa Aesar) and 63.1 mg sodium acetate (99.9 %, Alfa Aesar) were mixed in a flask with 25 mL methanol (99.9 %, Alfa Aesar), sealed under CO (99.99%, Air Liquide) at 55 °C for 24 h. Then

the flask was cooled down to room temperature, followed by adding 115.2 mg MWCNT and 14.2 mg MOF(Ce) into the flask under N_2 (99.99%, Air Liquide). The system was sealed under this condition with continuous stirring for 12 h. The solvent was evaporated at 80 °C under N_2. The obtained powder was dried at 60 °C overnight under air. The obtained catalyst, rinsed by ultra-pure water (18.2 MΩ cm^2, Millipore), was SMOF-1 sample. The SMOF-1 powder was heated at 50 °C under Ar (99.99 %, Air Liquide) for 60 min, followed by heat-treatment increasing the temperature at a heating rate of 10 °C min^{-1} from 50 to 400 °C or 900 °C and maintained at this temperature for 2h under Ar, noted as SMOF-2 and SMOF-3 samples, respectively. Finally, the powder was cooled down to room temperature under Ar. Thereafter, the powder was rinsed by ultra-pure water (18.2 MΩ cm, Millipore).

The synthesis of SCNTs samples was the same as that of SMOF system, except that no MOF(Ce) was added into the system during the synthesis. The protocol for heat-treatment was the same to that of SMOF. The as-prepared and heat-treated samples at 400 °C and 900 °C are noted as SCNT-1, SCNT-2 and SCNT-3, respectively.

The synthesis of SMOF-4 sample was the same as that of SMOF-1 sample, except that 125 mg of pre-treated support was added into the system during the synthesis. This support was prepared by heating the mixed MOF(Ce) and MWCNT at 900 °C under Ar for 2h.

The synthesis of SMOF-5 and SMOF-6 samples followed the same procedure to that of SMOF-3, except that 125 mg of Vulcan XC-72 and MWCNT-m were used as substrate materials. The preparation of MWCNT-m was as reported in literature [33].

2.2. Physical and chemical characterizations.

Powder X-ray diffraction patterns (*p*XRD) measurements of catalysts powders were performed on an EMPYREAN PANALYTICAL X-ray diffractometer using Cu K$_\alpha$ radiation (λ = 0.15406 nm). The XRD spectra were obtained using high resolution with the step-scanning mode, a narrow receiving slit (1/16°), and a counting time of 240 s per 0.05° from 12° to 120°. By referring to the Joint Committee on Powder Diffraction Standards International Center for Diffraction data (JCPDS-ICDD) database, the structural phase was identified. Prior to analysis, the 2θ and instrumental broadening for all the *p*XRD patterns were corrected by the pattern of LaB$_6$ measured at the same experimental condition. The lattice parameter, a_{fcc}, of catalysts was estimated from Equations (1) and (2).

$$d_{hkl} = \frac{\lambda}{2sin\theta} \qquad (1)$$

$$d_{hkl} = \frac{a_{fcc}}{\sqrt{h^2+k^2+l^2}} \qquad (2)$$

Where λ = 0.154056 nm, θ diffraction angle in radians, *hkl* Miller indices, and d*hkl* the interplanar distance. In this work, *a*, was the average value of calculations of 5 typical diffraction peaks belonging to Pt face centered cubic. Strain effect (ε), stacking fault (α) and crystallite size (*Lv*) were estimated based on the Williamson-Hall method, following the same calculation procedure in our previous works *via* Equation (3).[7, 34]

$$\frac{\beta cos\theta}{\lambda} = \frac{k}{L_v} + \frac{K_{hkl}}{a_{fcc}}\alpha + \frac{4sin\theta}{\lambda}\varepsilon \qquad (3)$$

Where β is the full-width at half-maximum (FWHM) of the diffraction peak, λ = 0.154056 nm, θ diffraction angle in radians, *k* is the Scherrer constant considering equal to 1, K(111) = 0.43, K(200) = 1, K(220) = 0.71, K(311) = 0.45 and K(222) = 0.43. Each diffraction peak was fitted with Pearson VII function. This function aids to obtain the parameters such as *a*, θ_{hkl} and full-

9

width at half-maximum experimental (FWHM, β_{exp}) applied at the Pawley method[35], equations (4) - (8).

$$I_C = \frac{I_{hkl}}{(1+\kappa \times \Delta\theta^2)^m} \qquad (4)$$

$$\kappa = \frac{4(2^{1/m}-1)}{\beta_{exp}^2} \quad (5)$$

$$I_C = I_{hkl}\left\{(1-m) \times \exp\left(-\ln 2 \times 4{\kappa_I}^2\right) + \frac{m}{1+4{\kappa_I}^2}\right\} \qquad (6)$$

$$\kappa_I = \frac{\Delta 2\theta}{\beta_{exp}} \qquad (7)$$

$$\Delta 2\theta = 2\theta_i - 2\theta_{hkl} \quad (8)$$

where I_C is the calculated profile intensity of a data point i in equation (8), I_{hkl} is the peak height. The κ, κ_I, θ_{hkl}, a, β_{exp}, and m constants were extracted by Leverberg-Marquardt algorithm implemented in equation (3) using Fityk (free software)[36]. The mean particle size was investigated by transmission electron microscopy (TEM) on a JEOL microscopy (JEM-2001). The samples were dispersed in ethanol, then a drop of such a solution was placed on a copper grid covered by carbon film and the ethanol was evaporated. For all the catalysts, the particle diameter in TEM images was evaluated by ImageJ free software. The particle size distribution histograms were obtained by 500 single and spherical nanoparticles (with diameter lower than 50 nm) counting on different TEM images. The composition and mass metal loading of the samples were evaluated using ICP-OES (Optima 2000 DV, Perkin-Elmer) technique. The metal mass was *ca*. 16 wt% of Pt and 2 wt% of Ce in SMOF-1 and SMOF-2, *ca*. 19 wt% of Pt and 2 wt% of Ce in SMOF-3, *ca*. 20 wt% of Pt in SCNT-1 and SCNT-2 sample, *ca*. 46 wt% of Pt in SCNT-3 sample. Photoemission data was acquired in a custom designed ultrahigh vacuum (UHV) system equipped with a VG MK II Escalab electron analyzer, working at a base pressure of 10^{-10} mbar. Core level photoemission spectra (Pt *4f* and Ce *4d*, pass energy 20 eV) were taken at room

temperature in normal emission using a non-monochromatized Mg K$_\alpha$ anode. Powder samples were suspended in ethanol and drop casted on conductive carbon tape. After drying in air, the samples were introduced in the ultrahigh vacuum system, outgassed for 1 h, and finally analyzed. There was no evidence for charging. The spectrometer energy calibration was carried out by using a gold sample (Au *4f* at 84 eV). The Pt *4f* photoemission lines were separated into three different chemical-shifted components (Pt^0, Pt^{2+} and Pt^{4+}), after Shirley background removal, to identify the predominant oxidation state of Pt. For the deconvolution of the peaks, Voigt shaped peaks were used, imposing a FWHM in the 1–1.5 eV range, except for the metallic Pt component where an asymmetrical shape was used. The C 1s peak was separated into five single chemical shifted components. An asymmetrical shape was used for the sp^2 component, whereas symmetrical Voigt functions were used for the sp^3 component and the oxygenated groups. Raman spectra were recorded on a Horiba Jobin Yvon Labram HR800UV Raman spectrometer, equipped with an Ar$^+$ laser (Melles Griot) as light source and with a CCD cooled detector. The laser source frequency was 514.5 nm line. And the obtained spectra were analyzed by Fityk free software.

2.3. Electrode preparation and electrochemical measurement in half-cell.

The electrochemical measurements in half-cell were performed in 0.1 M HClO$_4$ at 25 °C. The glassy carbon electrode (GCE) as rotating disk electrode (RDE) with 3 mm diameter (geometric surface of 0.071 cm^2), was used as the working electrode (WE), preliminary polished using alumina powder. The reference electrode was a reversible hydrogen electrode (RHE). And a piece of glassy carbon was used as counter electrode. 10 mg of catalytic powder was added into 0.25 mL Nafion$^®$ solution (5 wt %, Aldrich) and 1.25 mL isopropanol/ultra-pure water (1/3, v/v) to obtain an ink. 3 µL of the catalytic ink was then deposited onto the GCE used as WE. The deposit was further dried under air on RDE at a speed of 700 rpm. The reproducibility of the

11

deposition method used in this study was checked for 10 deposits on RDE. The obtained active surface values based on hydrogen underpotential deposition surface area was 2.99 ± 0.99 cm^2 for 10 ink deposits on WE, calculated from cyclic voltammograms (described later). Electrochemical measurements were recorded using an Autolab Potentiostat/Galvanostat and performed in a three-electrode standard electrochemical cell. 0.1 M HClO$_4$ aqueous solution was diluted from 70 % HClO$_4$ (Suprapur, Merck) with ultra-pure water. The WE surface was firstly electro-cleaned by performing 20 voltammetric cycles at 50 mV s^{-1} between 0.05 to 1.2 V vs. RHE to obtain stable cyclic voltammograms (CVs). CO-stripping voltammograms were performed using the following methodology. First, CO was adsorbed under a controlled potential (0.1 V vs. RHE) in a CO-saturated electrolyte for 10 min. Then the electrolyte was purged by bubbling N$_2$ for 30 min. Finally, CVs at a scan rate of 5 mV s^{-1} were performed in the CO free electrolyte in the potential interval ranging from 0.05 to 1.2 V vs. RHE. The ORR activity was evaluated by recording linear sweep voltammograms (LSVs) at a scan rate of 5 mV s^{-1} in the 1.0 - 0.2 V vs. RHE potential range in O$_2$-saturated (99.99%, Air Liquide) electrolyte using the RDE technique. The rotating rates of RDE for LSVs were 400, 900, 1600 and 2500 rpm. The kinetic current density was calculated with the Koutecky-Levich (K-L) Eq. (9) [37]:

$$\frac{1}{j} = \frac{1}{j_k} + \frac{1}{j_d} = \frac{1}{j_k} + \frac{1}{BC^0\omega^{1/2}} \qquad (9)$$

where j is the current density, jk the kinetic current density, j_d the diffusion current density, C^0 the concentration of molecular oxygen, ω the angular rate of rotating disk electrode. Linear fitting Eq. (9), j^{-1} vs. $\omega^{-1/2}$, j_d can be obtained from the slope and $\omega^{1/2}$. jk could be derived, using Eq. (9). The active surface area (cm^2) was calculated by the coulometry of the hydrogen under potential deposition (H$_{upd}$) or by the CO oxidation peak surface, using a charge of 210 and 420 µC cm^{-2},

respectively. The electrochemical surface area (ECSA), geometric surface area, ORR specific activity (SA), and mass activity (MA) are defined in Equations (10-13).

$$ECSA = \frac{Active\ surface\ area\ (m^2)}{Pt\ mass\ (g)} \qquad (10)$$

$$Geometric\ area = \frac{6000}{\rho d}\ (\rho = Pt\ density, d = mean\ particle\ size) \qquad (11)$$

$$SA = \frac{kinetic\ current\ (\mu A)}{Active\ surface\ (cm^2)}\ (12)$$

$$MA = \frac{kinetic\ current\ (mA)}{Pt\ mass\ (mg)}\ (13)$$

For accelerated durability tests (ADT), the WE was submitted to CVs cycles at a scan rate of 50 mV s^{-1} between 0.6 to 1.0 V *vs*. RHE in N$_2$-saturated electrolyte. Then 20 cycles of CV recorded at a scan rate of 50 mV s^{-1} between 0.05 to 1.2 V *vs*. RHE in N$_2$-saturated electrolyte to evaluate the active surface area of aged catalyst. Finally, LSVs were recorded at scan rate of 5 mV s^{-1} between 1.0 to 0.2 V *vs*. RHE in O$_2$-saturated electrolyte on RDE, to study the ORR kinetic.

3. Results and Discussion

3.1. Characterizations of SMOF and SCNT samples.

The power X-ray Diffraction (*p*XRD) patterns for all the catalysts are shown in **Figure 1a**. In the as-prepared and heat-treated SMOF and SCNT samples, only the face centered cubic Pt phase, namely (111), (200), (220), (311) and (222) can be identified. The peaks belonging to carbon phase can be found with comparison of *p*XRD pattern of MWCNT [38]. It is worth to note that no diffraction peaks associated to the pristine MOF(Ce) structure are observed in MOF samples. In fact, according to literatures [30, 39], MOF(Ce) loses its crystallinity but the highly porous

13

framework remains intact during the dehydration process starting at 50 °C. Essentially, the temperature in the synthesis of SMOF-1 is higher than 50 °C. This explains why no diffraction peak from MOF(Ce) can be observed in the pXRD patterns. Based on the analyses of pXRD patterns via Williamson-Hall method, **Figure 1b**, one can observe that $\beta cos\theta\lambda^{-1}$ (where β is the integral peak width, θ the angle, and λ the diffraction wavelength) values are non-linear with $4sin\theta\lambda^{-1}$. This indicates that the diffraction peak broadening is affected by the crystallite size (L_v), micro-strains (ε) and stacking faults (α). The calculated lattice parameter (a_{fcc}), L_v, ε and α, for all catalysts, are summarized in **Table 1**. For SMOF systems, the a_{fcc} decreases, whereas L_v increases upon heat-treatment. This infers that lattice strain effect is enhanced from SMOF-1 to SMOF-3 samples, together with increased crystallite size. The fact that α is reduced upon heat-treatment, suggests less intrinsic or extrinsic stacking at the planes of Pt nano-crystals after heat-treatment, possibly related to morphology change. On the other hand, ε value is decreased from ca. 1.17 % in the SMOF-1 to ca. 0.03 % in SMOF-3, which should be linked to increased L_v, strongly supporting a surface healing process during heat-treatment [40]. Indeed, on oxide supported Pt NPs, e.g., Pt/Cr-TiO$_2$ [41], a lattice strain effect was reported, which has been associated to the enhanced ORR activity. However, for SCNT systems, as listed in **Table 1**, the a_{fcc} value decreases from SCNT-1 to SCNT-2 sample and increases in SCNT-3 sample, indicating that the lattice strain effect induced by heat-treatment in SCNT-2 disappears in SCNT-3. Besides, the L_v value increases moderately from ca. 2.71 nm in SCNT-1 to ca. 5.25 nm in SCNT-2, but increases drastically in SCNT-3. Further, α values slightly decrease from SCNT-1 to SCNT-2, but sharply decrease in SCNT-3. All these results suggest a great change in the Pt particle morphology during heat-treatment for SCNT samples. The ε value is constant for SCNT samples during HT suggesting that the Pt surface remains intact.

From TEM images, one observes that in SMOF-1 (**Figure 2a**) Pt NPs are slightly agglomerated and are dispersed onto both MOF(Ce) framework and MWCNTs. Nanorods-like particles can also be found in this sample. The mean particle size (d) is *ca.* 2.0 ± 0.4 nm. After heat-treatment at 400 °C (**Figure 2b**), spherical NPs are still supported on both MOF(Ce), and MWCNT with d = 3.1 ± 0.9 nm. However, some Ce oxides fragments can be observed in this sample (see arrows in **Figure 2b**). Compared to SMOF-1, fewer nanorods-like particles can be observed in SMOF-2. For SMOF-3, several Pt agglomerations can be observed (not shown here) but most spherical Pt NPs are homogeneously dispersed onto MWCNT with d = 5.1 ± 2.2 nm (**Figure 2c**). No MOF(Ce) framework can be detected by TEM in this sample. Taking the thermal stability of MOF(Ce) structure into account, amorphous carbon mixed oxide should be formed from its decomposition at 900 °C [28, 30]. The Pt NPs in SMOF-3 are coated by a layer (*ca.* 0.5 − 1.0 nm, highlighted by arrows in **Figure 2c**), whose actual structure is hard to be revealed in absence of high resolution TEM images. Such a layer was found neither in SMOF-1 nor in SMOF-2 samples. However, using energy dispersive spectroscopy (EDS) mapping, see **Figure 2d**, we can stress that Pt, Ce and O are intimately connected and form a nanocomposite system. The morphological evolution is in good agreement with the Williamson-Hall analyses of pXRD patterns for SMOF samples during heat-treatment. The highest α value, in SMOF-1, should be associated to nanorods-like objects, since previous work revealed enhanced α value on nanorods-like for palladium with respect to spherical Pd NPs [34]. After heat-treatment, the number of nanorods is reduced, possibly inducing a decrease of α values. Moreover, the trend of L_v from pXRD corresponds to that of d from TEM (*cf.* **Table 1**). Concerning SCNT samples, it is very interesting to observe that the d of Pt NPs (*cf.* **Figure 3a-c**) increases from SCNT-1 (*ca.* 2.3 ± 0.4 nm) to SCNT-2 (*ca.* 4.8 ± 1.7 nm), and becomes huge due to Pt agglomerations detached from

MWCNT after HT-900 treatment (*ca*. 12 ± 9 nm) in SCNT-3. TEM images also reveal that NPs in SCNT-2 are less agglomerated than in SCNT-1, probably inducing a decrease of α.

In both SMOF and SCNT cases, the *d* value progression is in agreement with L_v, it is worth to note that the L_v are higher than *d* for all the catalysts. One observes in **Figure 2 and 3,** the presence of some non-spherical NPs (ex. nanorods, irregular agglomerates). These particles could not be taken into account in the determination of *d*. However, non-spherical (anisotropic) and agglomerated particles contribute to the diffraction peak broadening (β) of XRD diffraction peaks. The L_v was estimated from the Williamson-Hall method based on β, considering that the particles are isotropic, since it is hard to deconvolute the anisotropic or/and agglomeration impact from isotropic on β. Therefore, it is possible that the L_v is higher than *d* [42, 43]. For example, Said-Galiyev *et al* reported the L_v calculated from XRD is higher than *d* based on TEM, for both homemade and commercial Pt/C catalysts [44]. Weibel *et al* revealed the same phenomenon for TiO$_2$ particles [45]. In work of Langford *et al*, it was found that higher L_v than *d* occurs when the particle size distribution is wide [42]. Thus, the particle size evolution in SMOF with respect to SCNT systems, one can conclude a positive effect of MOF(Ce) in protecting Pt NPs from agglomeration at high temperature (e.g. 900 °C).

In order to obtain surface chemical composition of the catalysts, X-ray Photoemission Spectroscopy (XPS) data of the Pt *4f*, C *1s*, O *1s* and Ce *3d* photoemission lines for the SMOF and SCNT materials were taken. In **Figure 4** we summarize the most relevant data of the SMOF materials. The Pt *4f*, C *1s* and Ce *3d* peaks were separated into single chemical components in order to study any possible effect of both the support and the MOF(Ce) on the electronic properties of Pt NPs, as well as the effect of the thermal treatment at 900 °C under Ar atmosphere.

16

The Pt *4f* peak (**Figure 4a**) was separated into three different chemical-shifted components (Pt^0, Pt^{2+} and Pt^{4+}): as seen in **Table S1-1** in supporting information (SI), Pt^0 is the predominant oxidation state in all the Pt catalysts (around 79 – 84 %). However, all samples present a variable amount of oxidized species (Pt^{2+} and Pt^{4+}), deduced from the Pt *4f$_{7/2}$* peaks at a binding energy (BE) in the range 72.6 – 74.7 eV. The fact that there is a considerable amount of oxidized species is in general in tune with the relative small sizes of the Pt NPs. The treatment at 900 °C for SMOF-3 sample under Ar atmosphere results in a decrease of oxidized species, which can be related to the larger size of the Pt NPs (see TEM data) and also to a specific interaction with the Ce component obtained by the MOF(Ce) decomposition (see below) [31]. In the case of SCNT samples (not reported), the only significant change is associated to a small shift of the Pt *4f$_{7/2}$* peak of SCNT-3 toward lower BE with respect to SMOF-3 due to the relevant increase of the Pt NPs size, as already evidenced by the TEM analysis [46, 47].

The C *1s* peak (**Figure 4b**) of the investigated SMOF samples was separated into five single chemical shifted components. The most intense peak, centered at 284.4 eV, is associated to graphitic carbon (C sp^2), while the peak centered at 285.3 eV is associated to sp^3 hybridized carbon atoms (C sp^3). The samples also show peaks at 286.5, 288 and 289.1 eV, attributed to ternary alcohols, carbonyl and carboxylic groups, respectively (see **Table S1-2**). The treatments at 900 °C resulted in the reduction of the surface oxygenated species.

Ce *3d* XPS line is usually rather complex because it is characterized by the contribution of several initial and final states for each oxidation state of Cerium (Ce^{3+} and Ce^{4+}) [48]. The XPS pattern observed in **Figure 4c** is only compatible with the complete absence of Ce^{4+}: the Ce *3d$_{5/2}$* peak can be fitted with two components, at 882.1 and 886.2 eV, both associated to Ce^{3+} (**Table**

S1-3). These two components are assigned to two different final states where the $4f^1$ and $4f^2$ configurations are strongly mixed. No component associated to Ce^{4+} was used in the fit because the absence of a separate peak at around 916 eV is indicative of the absence of Ce^{4+} species. The analysis of SMOF-3 sample subjected to the treatment at 900 °C indicates that the structure of the Ce electronic state is slightly modified with respect to SMOF-1, in any case being absent of any fingerprint from Ce^{4+}: the two components associated to the different final states have different relative intensities (see the fitting in **Figure 4c** and **Table S1-3**), indicating small differences in the coordination of the Ce^{3+} ions, even if the difference cannot be easily rationalized. We can propose (see below) to associate such a change to the passage from Ce^{3+} ions attached to the MOF to Ce^{3+} associated to reduced ceria (CeO_x) in contact with the Pt NPs. In fact, the tendency of CeO_x to interact with Pt surfaces has been demonstrated by rigorous surface science studies on CeO_x/Pt(111) model systems, where the existence of ultrathin CeO_x layers on the Pt surface has been observed [49].

One can thus conclude from XPS that a nanocomposite formed by CeO_x, porous carbon and Pt NPs is present after the heat treatment at 900 °C in samples prepared by carbonyl chemical route adopting sacrificial MOF(Ce). A mechanism of the formation of such nanocomposite in SMOF-3 could be attempted as follows: in SMOF-1, the MOF(Ce) framework plays a role as substrate to support the Pt NPs. In this case the full coordination of the Ce^{3+} ions within the MOF framework is avoiding the oxidation to Ce^{4+} and the direct interaction with Pt. After heat treatment at 900 °C in Ar, the MOF framework is totally destroyed, forming a Pt/CeO_x/C(porous carbon+MWCNT) nanocomposite where porous carbon is somehow embedding the metallic components. We can suggest that at this stage the PtO_x layer around the Pt NPs is transformed into Pt/CeO_x. Interestingly enough, the porous carbon matrix fully protects the Ce^{3+} from full oxidation. This is

18

a quite unique behavior because the tendency of Ce^{3+} to form Ce^{4+} is rather high and even small traces of oxygen in standard Ar would be sufficient to partially oxidize Ce^{3+} in absence of such a protection.

3.2.   Surface electrochemistry for SMOF and SCNT samples.

The surface electrochemistry of SMOF and SCNT samples was firstly studied by cyclic voltammetry (CV) and the results are reported in **Figure 5**. The electrochemical surface area (ECSA) was calculated from the hydrogen under-potential deposition (H_{upd}) region. **Figure 5a** shows that the ECSA(H_{upd}) increases with the heat treatment, that is, from SMOF-1 (*ca*. 48 $m^2\,g^{-1}$) to SMOF-3 (*ca*. 72 $m^2\,g^{-1}$) (**Table S2**). It should be noted that the ECSA(H_{upd}) increases with the heat treatment, whereas the geometric area calculated from the average particle size decreases (see **Figure 2** and **Table S2**). This contradictory effect could be explained by the better dispersion of the Pt NPs obtained after the decomposition of the MOF(Ce) during the heat treatment at 900 °C, as seen by TEM. The presence of the CeO_x in SMOF-3 should promote the hydrogen adsorption-desorption of Pt NPs surfaces. It was reported that more H atoms can be adsorbed per Pt atom in cerium oxide supported Pt catalyst [11]. On the other hand, the electroactive surface area determined for CNT samples from the H_{upd} region (**Figure 5b**) decreases with the heat treatment due to the agglomeration of the Pt NPs with the heat treatment (**Table S2**). The low ECSA (H_{upd}) calculated for the SCNT-3 sample is attributed to the loss of the carbon support (*cf*. Pt mass of SCNT-3 in experimental section) during the heat treatment, leading to the total agglomeration of Pt NPs (*cf*. TEM images in **Figure 3c**). Besides, compared with the barely changed capacitance in SMOF samples, the double-layer behavior of SCNTs is not constant, probably suggesting deterioration of carbon support. These results reveal that the

19

presence of MOF(Ce) could stabilize and avoid the agglomeration of Pt NPs during heat-treatments.

To further understand the role of MOF(Ce) precursor, CO-stripping voltammograms were performed. All the synthesized SMOF samples (**Figure 5c**) showed two CO oxidation peaks at around 0.68 V and 0.76 V, respectively. The multi-peaks in CO-stripping have been associated in the literature to various aspects, such as Pt NPs size, [50, 51] facets [52, 53] and/or agglomeration [54] effects. Among them, the size effect should be negligible, since the peak shape and potential is barely changed with the increase of particle size, *cf*. SMOF-1 and SMOF-2 in **Figure 5c**. Taking into account the morphology and distribution of the Pt NPs deduced from TEM, the two peaks could be related to the CO oxidation on Pt NPs interacting with different substrate domains. According to the literature, peak 1 could be attributed to the CO-oxidation on Pt NPs interacting with the graphitic domain (sp^2) of MWCNT and/or with CeO_x [33, 55]. whereas, peak 2 could be associated to Pt NPs interacting with disordered carbon (sp^3) domain [33]. For SMOF-3, the intensity ratio $\frac{Peak\ 1}{Peak\ 2}$ increases, which could indicate that the peak 1 is related to Pt-CeO_x interaction rather than Pt-sp^2 interaction. In the literature, the enhancement of $\frac{Peak\ 1}{Peak\ 2}$ ratio, representing an increased Pt-sp^2 interaction with respect to Pt-sp^3, has been attributed to the decrease of the $\frac{I_D}{I_G}$ (intensity of disordered/graphite domains) ratio obtained *via* Raman spectroscopy [33]. However, as shown in **Figure 5e**, the Raman spectra show $\frac{I_D}{I_G}$ values of *ca*. 1.1 for SMOF-3, slightly increased with respect to those obtained for MWCNT (*ca*. 1.0) and SMOF-1 (*ca*. 1.0). This result would exclude the influence of Pt-sp^2 interaction on peak 1. Therefore, the Pt-CeO_x interaction should be responsible for the enhancement of the electro-oxidation of CO at lower potentials. For peak 2 in SMOF-3, the peak shape becomes larger, possibly associated to

enhanced Pt-sp^3 interaction favored within the CeO$_x$-C composite matrix, because the amount of disordered carbon increased (*cf.* $\frac{I_D}{I_G}$ ratio in **Figure 5e**) due to the decomposition of the MOF precursor. The ECSA values (**Table S2**) for SMOF samples, deduced from CO-oxidation peak surface, increase upon heating temperature. The ECSA value of SMOF-3 is still higher than the geometric area, suggesting that the adsorption of CO on Pt surface is promoted. For SCNT samples (**Figure 5d**), the CO oxidation peak shape and potential is basically the same in SCNT-1 and SCNT-2 samples, though their particle size values are different, excluding the particle size effect towards CO-stripping for SCNT samples. It can be seen that the potential and shape of peak 1 for SCNT-(1-2) are different from SMOF-3, supporting the Pt/oxide interaction in SMOF-3. For SCNT-3, the $\frac{I_D}{I_G}$ ratio in Raman spectra (**Figure 5e**) shows sp^3 domain of carbon is dominant rather than sp^2 domain. Therefore, the phenomenon of missing peak 2 with the negatively shifted peak 1 assesses the CO oxidation is done on larger particles detached from CNT supporting material (as seen from TEM).

3.3. Oxygen reduction reaction on SMOF and SCNT samples in half-cell.

The activity of the freshly prepared electrocatalysts towards ORR activity was then investigated; the linear sweep voltammograms (LSV) are reported in **Figure 6**. A gradual shift of the half-wave potential (E$_{1/2}$) towards more positive potentials with the heating temperature is observed for SMOF samples (**Figure 6a**). This positive shift can be attributed to the formation CeO$_x$/C composite interacting with the Pt NPs. Conversely, for the SCNT samples (**Figure 6b**), a negative shift of E$_{1/2}$ was observed with the heating temperature. This effect can be associated to the Pt NPs agglomeration with the heat treatment.

In order to further investigate the ORR kinetics, the Tafel slope in the potential interval of 0.96 to 0.92 V was determined. For the SMOF samples (**Figure 6c**), the slope decreases with the heating temperature (from *ca*. -76 mV dec^{-1} for SMOF-1 to *ca*. -52 mV dec^{-1} for SMOF-3), indicating that the Pt/CeO$_x$/C system has also a positive effect on the ORR kinetics. For the SCNT samples (**Figure 6d**), the slope decreases with the heating temperature but the values are higher than the one obtained for the commercial Pt/C (JM) catalyst.

Figure 6e summarizes the surface specific (SA) and mass activity (MA) for ORR. As seen above, all the SCNT samples and SMOF-1 show a lower activity than the commercial Pt/C (JM) catalyst. However, both SMOF-2 and SMOF-3 have a better performance, with the last one showing higher values than those targeted by the DOE-2015/2017 (Department of Energy, USA) (SA = 770 μA cm^{-2}$_{Pt}$ and MA = 440 mA mg^{-1}$_{Pt}$ at 0.9 V vs RHE in half-cell) [56]. These results further highlight that the presence of CeO$_x$/C interacting with Pt has an important role in promoting the ORR process. Later on, to study the effect of CeO$_x$/C, SMOF-3 was subjected to an accelerated durability test (ADT) for the ORR stability in the potential interval of 0.6 V to 1.0 V. The commercial Pt/C (JM) catalyst was used as reference catalyst. The SCNT-2 samples were also subjected to the ADT for comparison to minimize the particle size effect in ORR durability. The evolution of CVs and ORR polarization curves are shown in **Figure S3**. The loss of electrochemical active area and activity with the number of cycles is depicted in **Figure 6f**. For the commercial Pt/C (JM) and SCNT-2 samples, the active surface area (H$_{upd}$) and kinetic current density, j_k, decreases with the cycles, and this is reflected in a loss of activity towards ORR. However, the SMOF-3 sample is very stable. TEM images of the SMOF-3 sample after the ADT (**Figure 7a**) confirm that there is no agglomeration of the Pt NPs during the cycling treatment and the average particle size does not change. Besides, one can notice that the layer outside the Pt

NPs in SMOF-3 becomes thinner after ADT. Conversely, for SCNT-2 catalyst, the TEM (**Figure 7b**) shows that morphology and particle size Pt NPs are changed because of the formation of agglomerations after ADT. Considering the results of CO-stripping, these facts reveal that the interaction of Pt-CeO$_x$, induced by the unique morphology of Pt/CeO$_x$/C composite should be responsible for ORR stability improvement.

3.4. SMOFs and SCNTs as cathodes in H$_2$/O$_2$ micro laminar flow fuel cell (μLFFC).

The cathodic performance of SMOF and SCNT catalysts were evaluated *via* μLFFC [57, 58]. The commercial Pt/C (JM) catalyst was also tested in the same system for comparison. All data in **Figure 8** were iR-drop corrected (cf. procedure in SI). **Figure 8a** shows that a better performance of the μLFFC system is obtained when the cathode side contains SMOF-3, as expected among other SMOFs, and those labeled SCNTs (**Figure 8b**) and commercial Pt/C (JM) catalysts. The performance at the anode side is similar since the commercial Pt/C (JM) catalyst was used in all experiments (cf. Section 4, SI). The cell voltage characteristics as well as the power curves are shown in **Figure 8c-d**, and as expected the highest power density is obtained with SMOF-3 in the μLFFC system. At a current density of *ca*. 200 mA cm^{-2}, the power density on SMOF-3 (*ca.* 129 mW cm^{-2}) is a factor of *ca.* $1.2 - 1.7$ higher than that of SMOF-1, SMOF-2, SCNT-1, SCNT-2 and Pt/C (JM). The cell voltage on SMOF-3 cathode attains 1.0 V. This value is higher than on the other cathode systems, *cf.* **Figure 8c-b**. Hence, SMOF-3, in μLFFC system, outperforms the other cathodes.

3.5. Investigation for the formation of Pt/CeO$_x$/C composite.

The high activity of Pt centers is due to the formation of Pt/CeO$_x$/C in SMOF-3 catalyst. In order to investigate this issue, the synthesis of Pt NPs deposited on the pre-treated MOF(Ce) mixed with MWCNT, noted as: SMOF-4, was performed. It shows a different surface electrochemical

behavior, as contrasted in **Figure 9a-b**. The shape of H_{upd} region and the double-layer behavior in CVs, as well as CO-oxidation peak shape and potential, are different from that of SMOF-3. It is worth to be noted that the H_{upd} and CO-oxidation peak surface area for both catalysts are very similar, implying similar amount of Pt active sites. Then again the LSVs (**Figure 9c**) illustrates that the ORR activity on SMOF-3 outperforms that of SMOF-4. This should be associated with the special morphology and interaction of CeO_x/C moieties with Pt active sites in SMOF-3 that shows an enhanced ORR activity with respect to SMOF-4. It demonstrates also that the formation of $Pt/CeO_x/C$ composite is an *in-situ* procedure.

Additionally, the carbon, as support, plays an important role in the synthesis of SMOF-3 catalyst. In order to investigate the support effect, besides MWCNT which is used for the synthesis of SMOF-(1-3) and SCNT samples [32], two different carbon were used in the synthesis of $Pt/CeO_x/C$ composites: Vulcan XC-72 [59] (SMOF-5) and MWCNT-m [33] (SMOF-6), *via* the same synthetic procedures. From the Raman spectra on these supports, **Figure 9e**, it is clear that the $\frac{I_D}{I_G}$ value follows the trend: XC-72 (*ca.* 2.1) [33] > MWCNT (*ca.* 1.0) > MWCNT-m (*ca.* 0.5) [33]. Then the CVs, depicted in **Figure 9d**, show that the SMOF-3 gives much larger H_{upd} surface area than SMOF-5 and SMOF-6 samples. The ORR polarization curves, in **Figure 9f**, confirm that the best catalyst is achieved with MWCNT support: the SMOF-3 catalyst. Hence, the formation of highly active $Pt/CeO_x/C$ should also be related to the nature of carbon support.

4. Conclusions

Through this study, we explore the role of a MOF(Ce) as a sacrificial precursor during the synthesis of $Pt/CeO_x/C$ nanocomposite (SMOF-3), and compared to MOF-free samples. From the analysis of *p*XRD and TEM data, one can conclude that the impact of MOF was unique in

forming of CeO$_x$, intimately contacted to Pt surface, and protecting Pt NPs against agglomeration. The XPS reveals that CeO$_x$, derived from MOF(Ce), interact with Pt NPs, stabilizing Pt^0 and Ce^{3+} state in the nanocomposite. The surface electrochemistry of Pt/CeO$_x$/C nanocomposite is thus modified, showing promoted H and CO adsorption, thus higher Pt active surface area with respect to other SMOF, SCNT and commercial Pt/C (JM) catalyst. The CO-stripping analysis, together with Raman spectra, demonstrates strong interaction between Pt and CeO$_x$. The ORR activity on SMOF-3 catalyst was observed as highly enhanced with respect to SMOF, SCNT and Pt/C (JM) catalysts, outperforming DOE 2015/2017 target in half-cell. In addition, the ORR stability on SMOF-3, *via* ADT, was improved, in contrast to those oxide-free SCNT-2 and Pt/C (JM) samples. Finally, such an innovative composite was validated as cathode catalyst in a H$_2$/O$_2$ μLFFC system. Compared with other homemade and Pt/C (JM) cathodic catalysts, the cell power density was enhanced by a factor of *ca.* 1.2 − 1.7. All these facts assess the significant role of CeO$_x$, based on MOF(Ce) precursor, in the formation of Pt/CeO$_x$/C nanocomposite, leading to a modified Pt surface and resulting enhanced ORR kinetic and stability. This work has also demonstrated that the novel Pt/CeO$_x$/C nanocomposite can be *in-situ* prepared at high temperature (900 °C under inert gas) where both MWCNTs and porous carbon are key ingredients. Our study, indeed, extends the application of MOF materials in preparation of Pt-based nanomaterials for energy conversion.

ACKNOWLEDGMENTS

Mora-Hernandez for some experiments on µLFFC. The synthesis of Pt/CeOx/C composite was protected a patent (**WO2015144894A1**).

References

[1] W. Yu, M.D. Porosoff, J.G. Chen, Chem. Rev. (Washington, DC, U. S.), 112 (2012) 5780-5817.

[2] Y. Luo, N. Alonso-Vante, Electrochim. Acta, 179 (2015) 10.

[3] GreeleyJ, I.E.L. Stephens, A.S. Bondarenko, T.P. Johansson, H.A. Hansen, T.F. Jaramillo, RossmeislJ, ChorkendorffI, J.K. Nørskov, Nat Chem, 1 (2009) 552-556.

[4] S.J. Yoo, K.-S. Lee, S.J. Hwang, Y.-H. Cho, S.-K. Kim, J.W. Yun, Y.-E. Sung, T.-H. Lim, Int. J. Hydrogen Energy, 37 (2012) 9758-9765.

[5] M. Escudero-Escribano, A. Verdaguer-Casadevall, P. Malacrida, U. Grønbjerg, B.P. Knudsen, A.K. Jepsen, J. Rossmeisl, I.E.L. Stephens, I. Chorkendorff, J. Am. Chem. Soc., 134 (2012) 16476-16479.

[6] M.K. Jeon, P.J. McGinn, J. Power Sources, 196 (2011) 1127-1131.

[7] Y. Luo, A. Habrioux, L. Calvillo, G. Granozzi, N. Alonso-Vante, ChemPhysChem, 15 (2014) 2136-2144.

[8] K.G. Nishanth, P. Sridhar, S. Pitchumani, Electrochem. Commun., 13 (2011) 1465-1468.

[9] P. Hernandez-Fernandez, F. Masini, D.N. McCarthy, C.E. Strebel, D. Friebel, D. Deiana, P. Malacrida, A. Nierhoff, A. Bodin, A.M. Wise, J.H. Nielsen, T.W. Hansen, A. Nilsson, E.L. StephensIfan, I. Chorkendorff, Nat. Chem., 6 (2014) 732-738.

[10] Y. Luo, A. Habrioux, L. Calvillo, G. Granozzi, N. Alonso-Vante, ChemCatChem, 7 (2015) 1573-1582.

[11] P. Bera, A. Gayen, M.S. Hegde, N.P. Lalla, L. Spadaro, F. Frusteri, F. Arena, J. Phy. Chem. B, 107 (2003) 6122-6130.

[12] N. Alonso-Vante, Fuel Cells, 6 (2006) 182-189.

[13] L. Yang, S. Kinoshita, T. Yamada, S. Kanda, H. Kitagawa, M. Tokunaga, T. Ishimoto, T. Ogura, R. Nagumo, A. Miyamoto, M. Koyama, Angew. Chem., 122 (2010) 5476-5479.

[14] J.-R. Li, R.J. Kuppler, H.-C. Zhou, Chem. Soc. Rev., 38 (2009) 1477-1504.

[15] Y. Qiu, H. Deng, S. Yang, J. Mou, C. Daiguebonne, N. Kerbellec, O. Guillou, S.R. Batten, Inorg. Chem., 48 (2009) 3976-3981.

[16] S. Freslon, Y. Luo, G. Calvez, C. Daiguebonne, O. Guillou, K. Bernot, V. Michel, X. Fan, Inorg. Chem., 53 (2014) 1217-1228.

[17] X. Yi, K. Bernot, F. Pointillart, G. Poneti, G. Calvez, C. Daiguebonne, O. Guillou, R. Sessoli, Chemistry – A European Journal, 18 (2012) 11379-11387.

[18] J. Lee, O.K. Farha, J. Roberts, K.A. Scheidt, S.T. Nguyen, J.T. Hupp, Chem. Soc. Rev., 38 (2009) 1450-1459.

[19] Y. Fu, D. Sun, Y. Chen, R. Huang, Z. Ding, X. Fu, Z. Li, Angew. Chem., 124 (2012) 3420-3423.

[20] C. Wang, Z. Xie, K.E. deKrafft, W. Lin, J. Am. Chem. Soc., 133 (2011) 13445-13454.

[21] H.-L. Jiang, Q. Xu, Chem. Commun. (Cambridge, U. K.), 47 (2011) 3351-3370.

[22] A.K. Singh, Q. Xu, ChemCatChem, 5 (2013) 3000-3004.

[23] C. Wang, K.E. deKrafft, W. Lin, J. Am. Chem. Soc., 134 (2012) 7211-7214.

[24] C.O. Ania, M. Seredych, E. Rodriguez-Castellon, T.J. Bandosz, Appl. Catal., B, 163 (2015) 424-435.

[25] J. Shui, C. Chen, L. Grabstanowicz, D. Zhao, D.-J. Liu, Proceedings of the National Academy of Sciences, 112 (2015) 10629-10634.

[26] T.B. Čelič, M. Grilc, B. Likozar, N.N. Tušar, ChemSusChem, 8 (2015) 1703-1710.

[27] Q. Li, P. Xu, W. Gao, S. Ma, G. Zhang, R. Cao, J. Cho, H.-L. Wang, G. Wu, Adv. Mater. (Weinheim, Ger.), 26 (2014) 1378-1386.

[28] J.-W. Jeon, R. Sharma, P. Meduri, B.W. Arey, H.T. Schaef, J.L. Lutkenhaus, J.P. Lemmon, P.K. Thallapally, M.I. Nandasiri, B.P. McGrail, S.K. Nune, ACS Appl. Mater. Interfaces, 6 (2014) 7214-7222.

[29] M. Jahan, Q. Bao, K.P. Loh, J. Am. Chem. Soc., 134 (2012) 6707-6713.

[30] Y. Luo, G. Calvez, S. Freslon, C. Daiguebonne, T. Roisnel, O. Guillou, Inorg. Chim. Acta, 368 (2011) 170-178.

[31] T. Masuda, H. Fukumitsu, K. Fugane, H. Togasaki, D. Matsumura, K. Tamura, Y. Nishihata, H. Yoshikawa, K. Kobayashi, T. Mori, K. Uosaki, J. Phy. Chem. C, 116 (2012) 10098-10102.

[32] A. Orfanidi, M.K. Daletou, S.G. Neophytides, Appl. Catal., B, 106 (2011) 379-389.

[33] J. Ma, A. Habrioux, C. Morais, A. Lewera, W. Vogel, Y. Verde-Gómez, G. Ramos-Sanchez, P.B. Balbuena, N. Alonso-Vante, ACS Catal., 3 (2013) 1940-1950.

[34] Y. Luo, J.M. Mora-Hernández, L.A. Estudillo-Wong, E.M. Arce-Estrada, N. Alonso-Vante, Electrochim. Acta, 173 (2015) 771-778.

[35] R.E. Dinnebier, S.J.L. Billinge (Eds.), (RSC publishing (2008)).

[36] M. Wojdyr, J. Appl. Crystallogr., 43 (2010) 3.

[37] A.J. Bard, L.R. Faulkner, Electrochemical Methods: Fundamentals and Applications, Second Edition ed., John Wiley&Sons, New York, 2001.

[38] L. Wang, P. Yu, L. Zhao, C. Tian, D. Zhao, W. Zhou, J. Yin, R. Wang, H. Fu, Sci. Rep., 4 (2014).

[39] Y. Luo, PhD thesis, INSA de Rennes (2012).

[40] W. Vogel, L. Timperman, N. Alonso-Vante, Appl. Catal. A, 377 (2010) 167-173.

[41] J.-H. Kim, S. Chang, Y.-T. Kim, Appl. Catal., B, 158–159 (2014) 112-118.

[42] J.I. Langford, D. Louer, P. Scardi, J. Appl. Crystallogr., 33 (2000) 964-974.

[43] D. Chataigne, Combined Analysis, John Wiley & Sons2010.

[44] E. Said-Galiyev, A. Nikolaev, E. Levin, E. Lavrentyeva, M. Gallyamov, S. Polyakov, G. Tsirlina, O. Petrii, A. Khokhlov, J. Solid State Electrochem., 15 (2011) 623-633.

[45] A. Weibel, R. Bouchet, F. Boulc, P. Knauth, Chem. Mater., 17 (2005) 2378-2385.

[46] Y. Takasu, N. Ohashi, X.G. Zhang, Y. Murakami, H. Minagawa, S. Sato, K. Yahikozawa, Electrochim. Acta, 41 (1996) 2595-2600.

[47] Y. Takasu, T. Iwazaki, W. Sugimoto, Y. Murakami, Electrochem. Commun., 2 (2000) 671-674.

[48] L. Artiglia, S. Agnoli, M.C. Paganini, M. Cattelan, G. Granozzi, ACS Appl. Mater. Interfaces, 6 (2014) 20130-20136.

[49] U. Berner, K.-D. Schierbaum, Physical Review B, 65 (2002) 235404.

[50] M. Nesselberger, S. Ashton, J.C. Meier, I. Katsounaros, K.J.J. Mayrhofer, M. Arenz, J. Am. Chem. Soc., 133 (2011) 17428-17433.

[51] F. Maillard, M. Eikerling, O.V. Cherstiouk, S. Schreier, E. Savinova, U. Stimming, Faraday Discuss., 125 (2004) 357-377.

[52] J. Solla-Gullón, F.J. Vidal-Iglesias, E. Herrero, J.M. Feliu, A. Aldaz, Electrochem. Commun., 8 (2006) 189-194.

[53] P. Urchaga, S. Baranton, C. Coutanceau, G. Jerkiewicz, Langmuir, 28 (2011) 3658-3663.

[54] F. Maillard, S. Schreier, M. Hanzlik, E.R. Savinova, S. Weinkauf, U. Stimming, Phys. Chem. Chem. Phys., 7 (2005) 385-393.

[55] J. Ma, E. Valenzuela, A.S. Gago, J. Rousseau, A. Habrioux, N. Alonso-Vante, J. Phy. Chem. C, 118 (2014) 1111-1117.

[56] M.K. Debe, Nature, 486 (2012) 43-51.

[57] A.S. Gago, Y. Gochi-Ponce, Y.-J. Feng, J.P. Esquivel, N. Sabaté, J. Santander, N. Alonso-Vante, ChemSusChem, 5 (2012) 1488-1494.

[58] L. Timperman, A.S. Gago, N. Alonso-Vante, J. Power Sources, 196 (2011) 4290-4297.

[59] H. Yang, N. Alonso-Vante, J.-M. Léger, C. Lamy, J. Phy. Chem. B, 108 (2004) 1938-1947.

Caption of figures.

Figure 1. (a) pXRD patterns, (b) Williamson-Hall plots for SMOFs and SCNTs systems. Empty symbols represent the 5 Bragg peaks data, and the filled ones the fitted data.

Figure 2. TEM images and particle size distribution for (a) SMOF-1, (b) SMOF-2, (c) SMOF-3. (d) EDS mapping for SMOF-3. Insets: higher magnification of TEM image for SMOF samples.

Figure 3. TEM images and particle size distribution for (a) SCNT-1, (b) SCNT-2, (c) SCNT-3. Insets: higher magnification of TEM image for SCNT samples.

Figure 4. (a) Pt *4f*, (b) C *1s* and (c) Ce *3d* XPS spectra, as well as the separation of the Pt *4f*, C *1s* and Ce *3d* regions into single chemical components, for the SMOF samples.

Figure 5. CVs (a, b) recorded at scan rate of 50 mV s^{-1}; and CO-stripping voltammograms (c, d) at scan rate of 5 mV s^{-1} in HClO$_4$, for SMOFs (a,c), and SCNTs (b,d) samples. (e) Raman spectra for MWNCT, SMOF and SCNT samples.

Figure 6. LSVs recorded at scan rate of 5 mV s^{-1} in O$_2$-saturated HClO$_4$ for (a) SMOFs and (b) SCNTs, at 25 °C at a rotation rate of 900 rpm. Mass-transfer corrected Tafel plots, derived from ORR polarization curves for (c) SMOFs and (d) SCNTs samples. (e) Mass and surface specific activity for SMOFs, SCNTs, Pt/C (JM) catalysts compared to the DOE 2015/2017 target; (f) Remaining H$_{upd}$ and j_k (@ 0.9 V *vs*. RHE) values obtained during ADT for SMOF-3, SCNT-2 and Pt/C (JM) catalysts.

Figure 7. TEM images and particles size distribution curves for (a) SMOF-3 and (b) SCNT-2 samples after ADT. Zoom of particles (insets).

Figure 8. (a – b) Corresponding representative anode and cathode polarization curves of a H_2/O_2 μLFFC; and (c – d) cell voltage and power density curves (iR-drop corrected). Pt/C (JM) catalyst was used as anode in all systems. All curves were recorded in 1.0 M $HClO_4$ at room temperature.

Figure 9. (a) CVs recorded at scan rate of 50 mV s^{-1} in N_2-saturated 0.1 M $HClO_4$; (b) CO-stripping voltammograms at scan rate of 5 mV s^{-1} in N_2-saturated 0.1 M $HClO_4$; (c) LSVs on RDE with rotating speed of 900 rpm at scan rate of 5 mV s^{-1} in O_2-saturated $HClO_4$ for SMOF-3 and SMOF-4. (d) CVs recorded at scan rate of 50 mV s^{-1} in N_2-saturated 0.1 M $HClO_4$ for SMOF-3, SMOF-5 and SMOF-6 samples; (e) Raman spectra for Vulcan XC-72, MWCNT and MWCNT-m materials. (f) LSVs on RDE with rotating speed of 900 rpm at scan rate of 5 mV s^{-1} in O_2-saturated $HClO_4$ for SMOF-3, SMOF-5 and SMOF-6 samples.

Figure 1.

Figure 2.

(a): SMOF-1
10 nm
100 nm
d = 2.0 ± 0.4 nm
5 nm

(b): SMOF-2
100 nm
10 nm
d = 3.1 ± 0.9 nm
5 nm

(c): SMOF-3
100 nm
10 nm
d = 5.1 ± 2.2 nm
5 nm

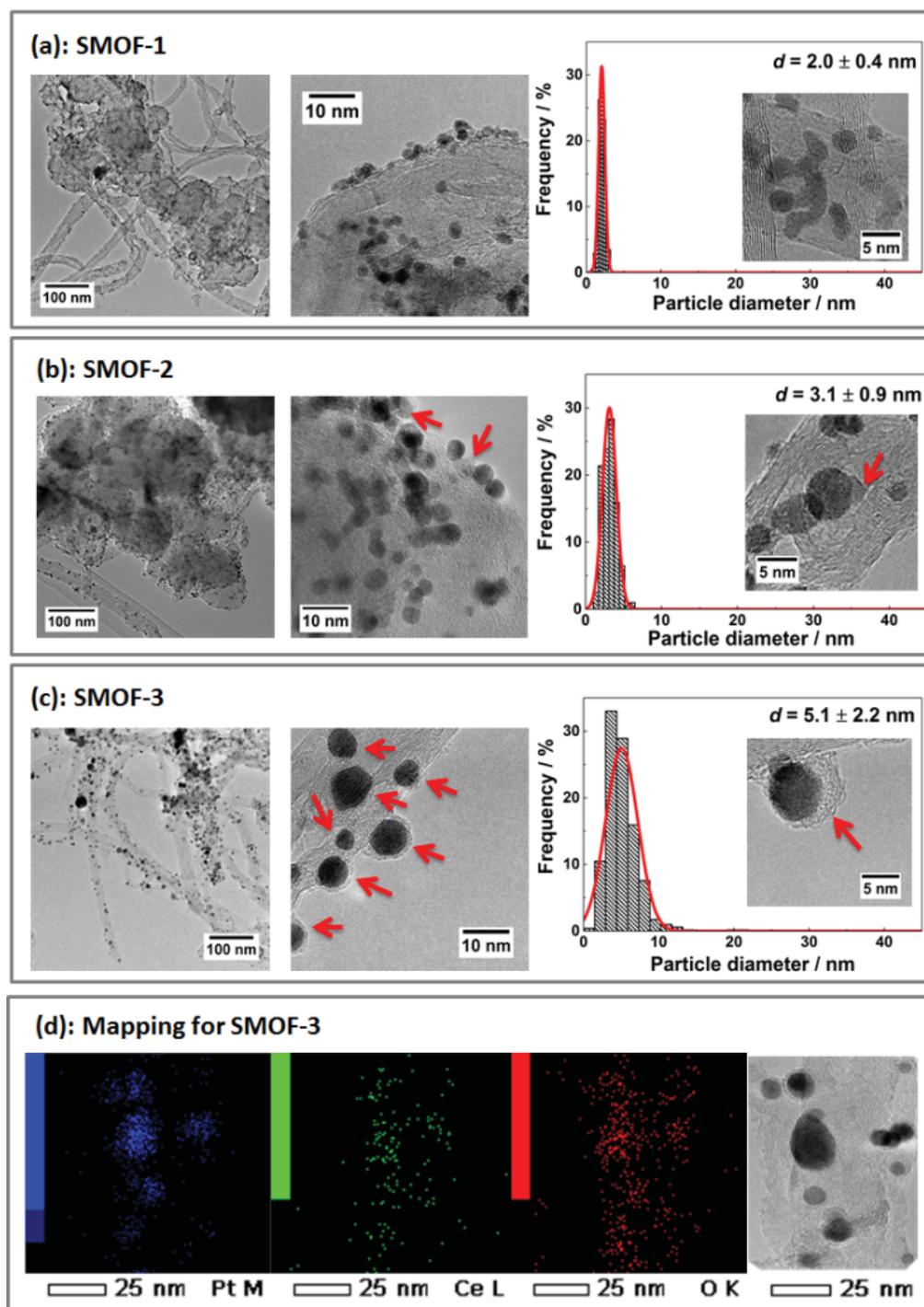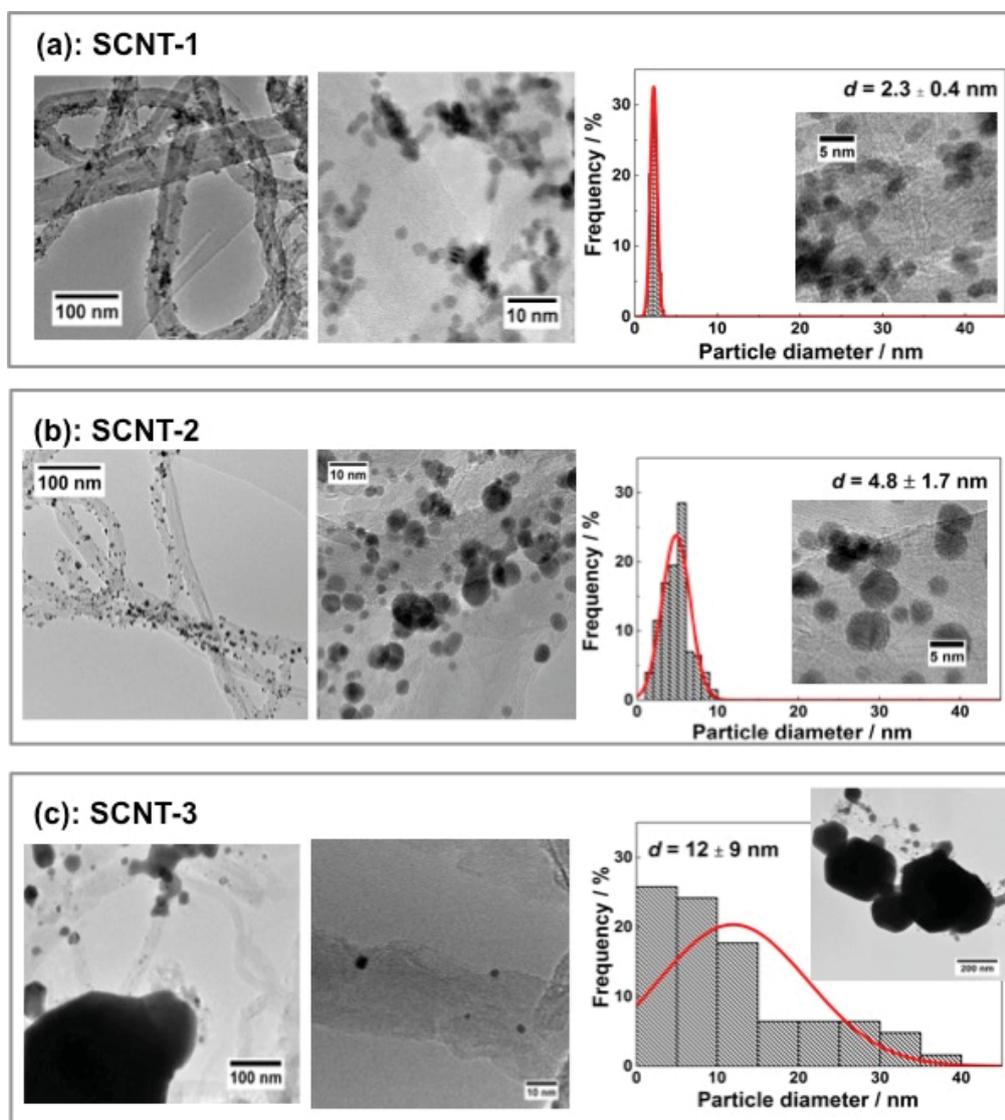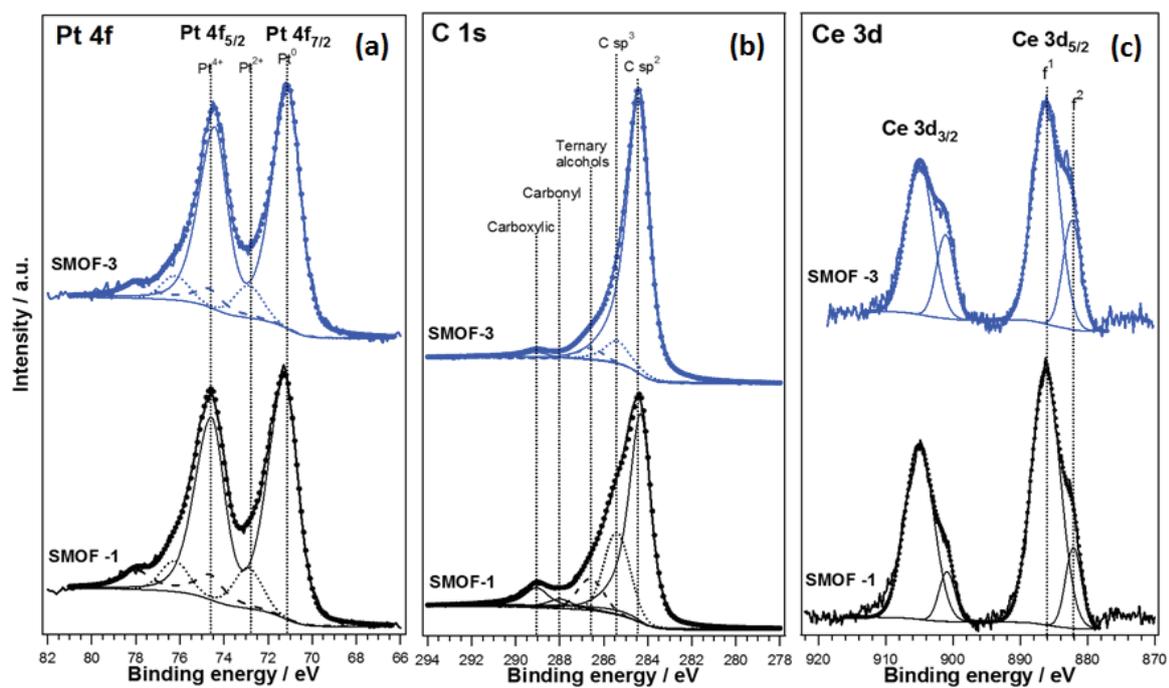(d): Mapping for SMOF-3
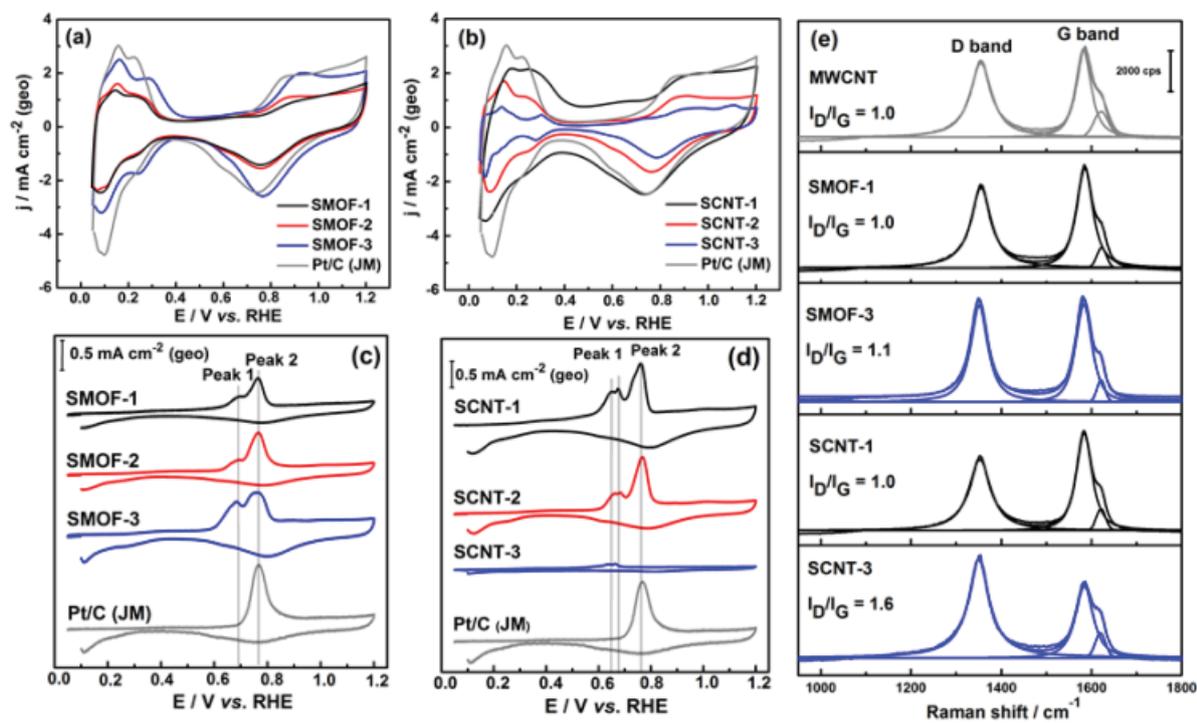25 nm   Pt M   25 nm   Ce L   25 nm   O K   25 nm
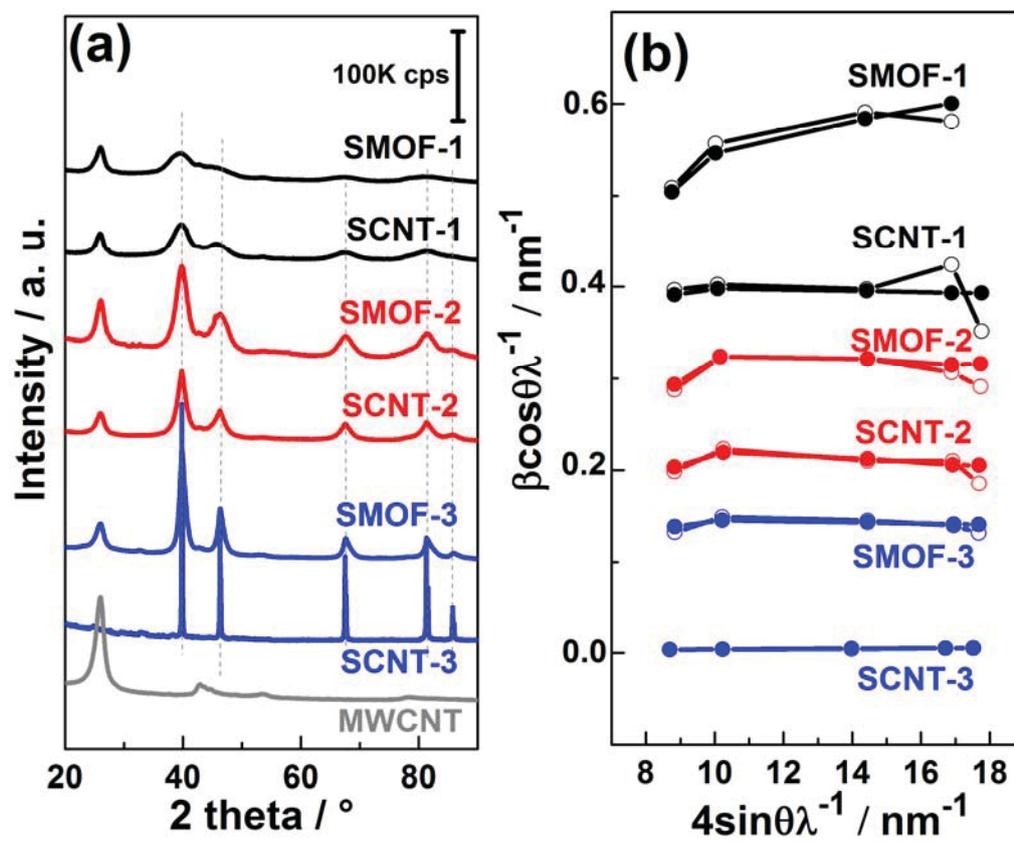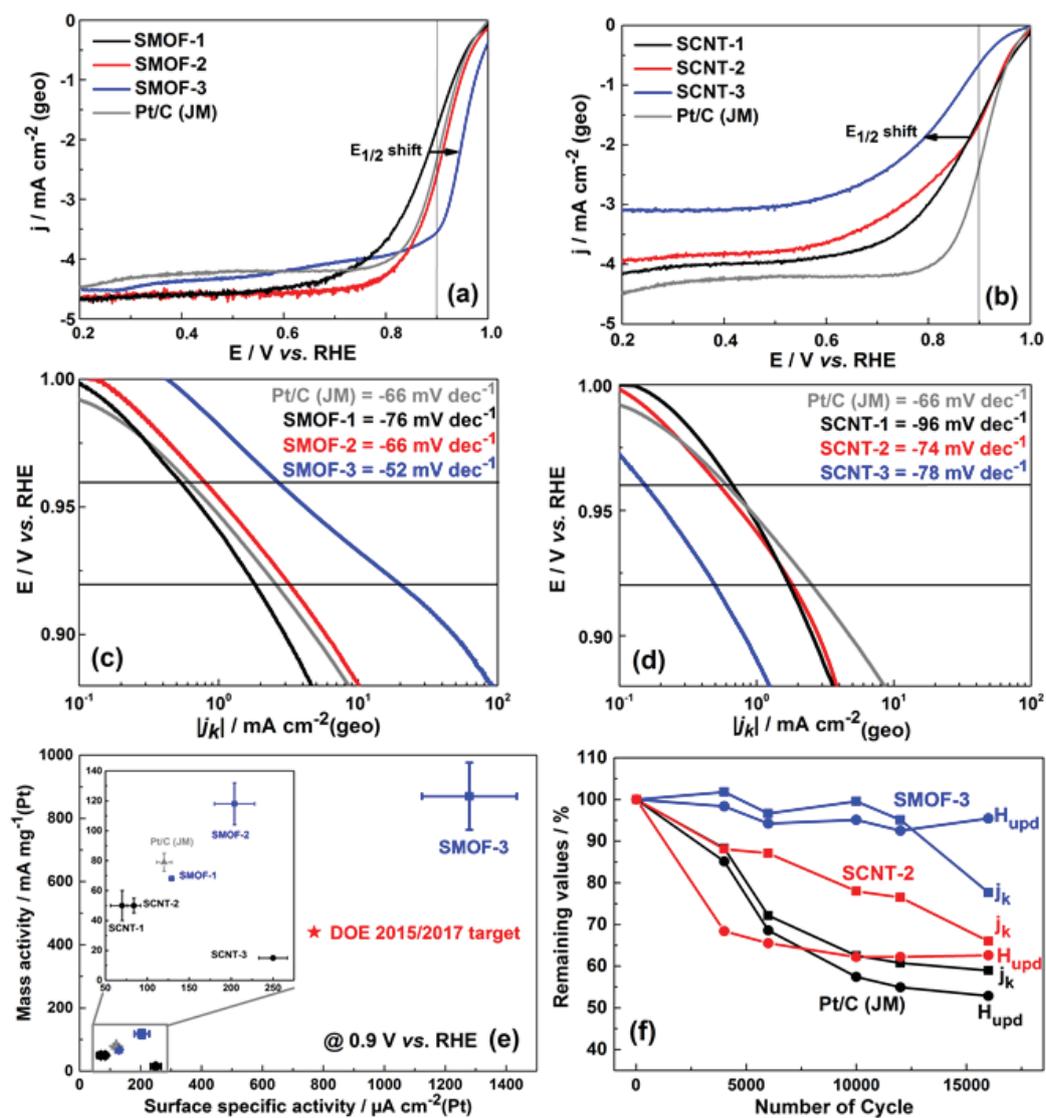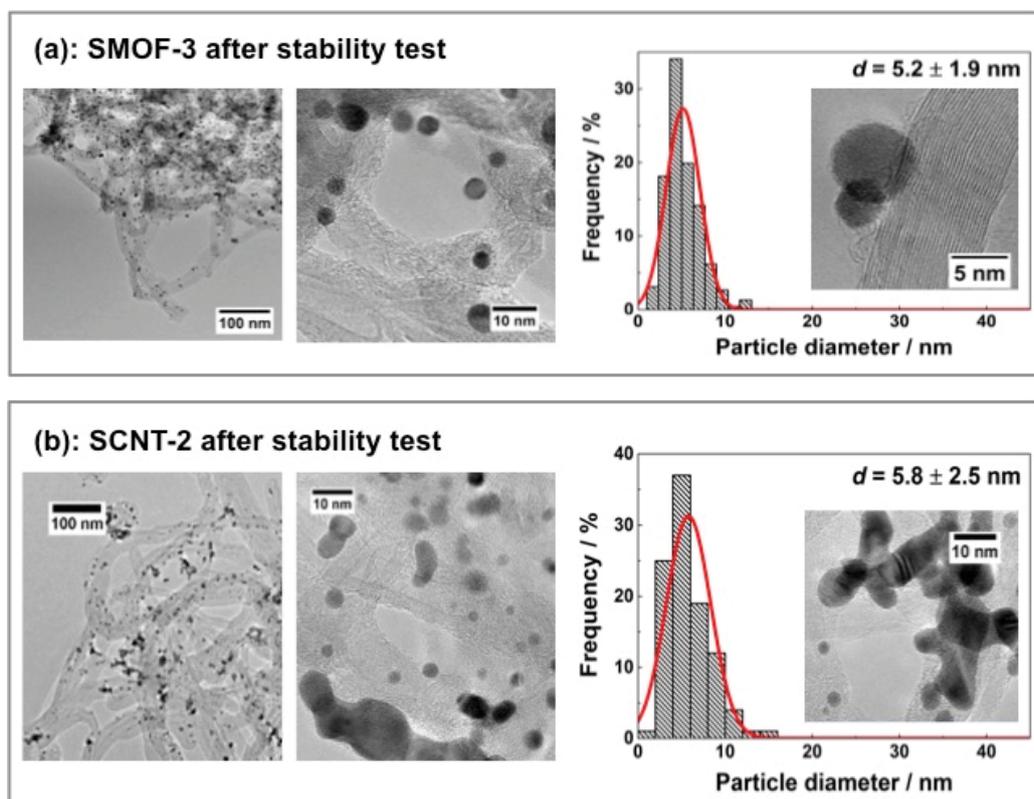
Figure 3.
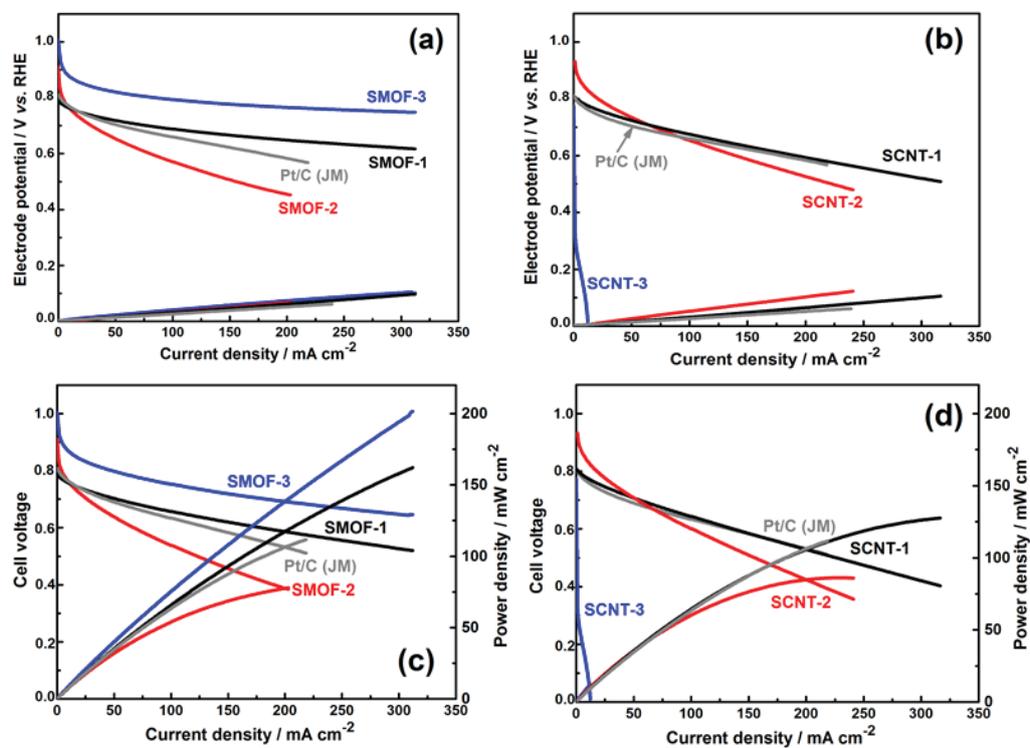
Figure 4.

Figure 5.

Figure 6.
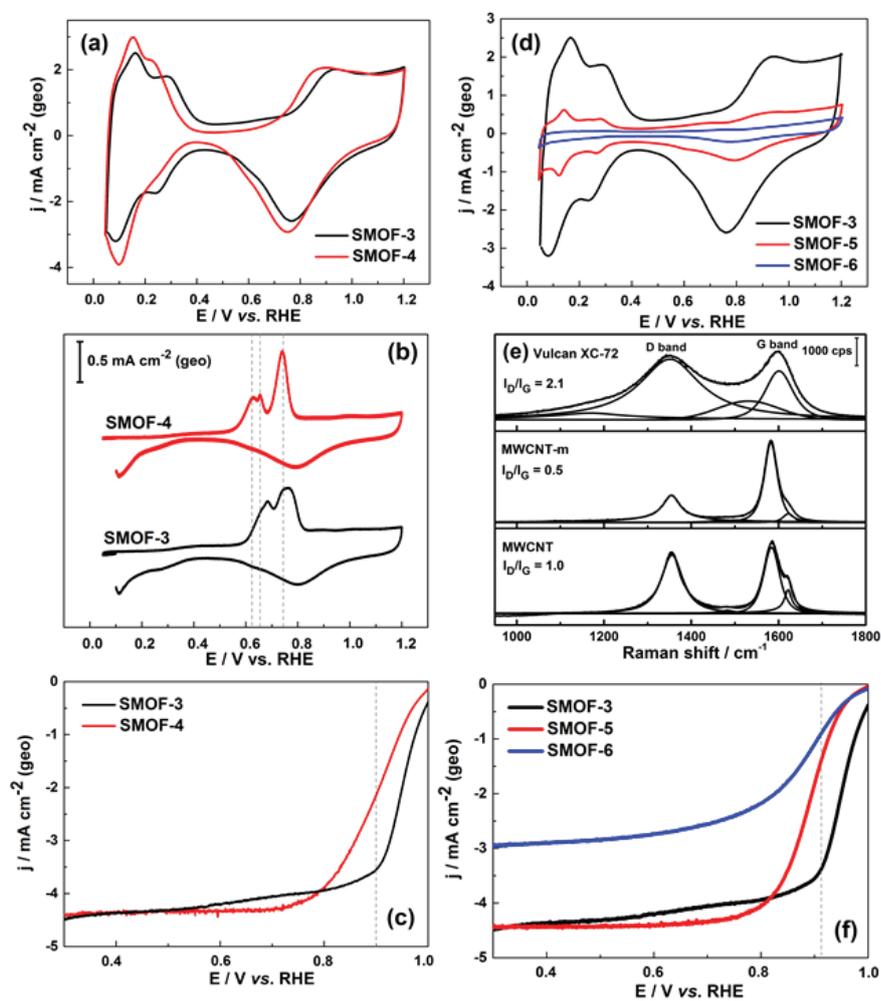
Figure 7.

Figure 8.

Figure 9.

Table 1. Parameters evaluated from *p*XRD patterns: lattice parameter (a_{fcc} / nm), crystallite size (L_v / nm), stacking fault (α / %), and micro-strain value (ε / %).

Sample	a_{fcc}	L_v	α	ε
SMOF-1	0.3942	2.63	1.95	1.17
SMOF-2	0.3922	3.98	1.85	0.25
SMOF-3	0.3915	7.65	0.45	0.03
SCNT-1	0.3928	2.71	1.43	0.02
SCNT-2	0.3915	5.25	1.05	0.02
SCNT-3	0.3972	625	0.001	0.02
Pt/C (JM) [a]	0.3927	4.6	-	0.023

(a) Data extracted from literature [44].